

# Lawrence Berkeley National Laboratory

## Recent Work

### Title

THE DECOMPOSITION OF CHROMIUM-TUNGSTEN SOLID SOLUTION

### Permalink

<https://escholarship.org/uc/item/2gn7p0r8>

### Author

Porter, David.

### Publication Date

1966

UCRL-16619

University of California

Ernest O. Lawrence  
Radiation Laboratory

THE DECOMPOSITION OF CHROMIUM-TUNGSTEN  
SOLID SOLUTION

TWO-WEEK LOAN COPY

This is a Library Circulating Copy  
which may be borrowed for two weeks.  
For a personal retention copy, call  
Tech. Info. Division, Ext. 5545

## **DISCLAIMER**

This document was prepared as an account of work sponsored by the United States Government. While this document is believed to contain correct information, neither the United States Government nor any agency thereof, nor the Regents of the University of California, nor any of their employees, makes any warranty, express or implied, or assumes any legal responsibility for the accuracy, completeness, or usefulness of any information, apparatus, product, or process disclosed, or represents that its use would not infringe privately owned rights. Reference herein to any specific commercial product, process, or service by its trade name, trademark, manufacturer, or otherwise, does not necessarily constitute or imply its endorsement, recommendation, or favoring by the United States Government or any agency thereof, or the Regents of the University of California. The views and opinions of authors expressed herein do not necessarily state or reflect those of the United States Government or any agency thereof or the Regents of the University of California.

Research and Development

UCRL-16619

UNIVERSITY OF CALIFORNIA  
Lawrence Radiation Laboratory  
Berkeley, California  
AEC Contract W-7405-eng-48

THE DECOMPOSITION OF CHROMIUM-TUNGSTEN  
SOLID SOLUTION

David Porter  
(M.S. Thesis)

January 1966



Table of Contents

I. Abstract . . . . .	1
II. Introduction . . . . .	2
III. Experimental Procedure . . . . .	8
A. Materials . . . . .	8
B. Sample Preparation . . . . .	8
C. Apparatus . . . . .	9
D. Techniques . . . . .	11
IV. Experimental Results . . . . .	12
A. X-Ray Diffraction Experiments . . . . .	12
B. Microhardness . . . . .	15
C. Metallography . . . . .	16
V. Discussion . . . . .	17
VI. Summary and Conclusions . . . . .	20
VII. Acknowledgments . . . . .	21
VIII. References . . . . .	22
IX. Figure Captions . . . . .	24

# THE DECOMPOSITION OF CHROMIUM-TUNGSTEN SOLID SOLUTION

David Porter

Inorganic Materials Research Division, Lawrence Radiation Laboratory,  
and Department of Mineral Technology, College of Engineering,  
University of California, Berkeley, California

January 1966

## ABSTRACT

The mechanism of solid solution decomposition within the chemical spinodal boundary was investigated for the tungsten-chromium system. Two alloys were solution treated, quenched, and aged at various temperatures inside the chemical spinodal boundary. It was concluded from x-ray and metallographic evidence that tungsten-chromium alloys do not decompose by a spinodal mechanism. The decomposition process was found to be one of nucleation and growth. A theoretical analysis provided answers which explained the behavior of this alloy system.

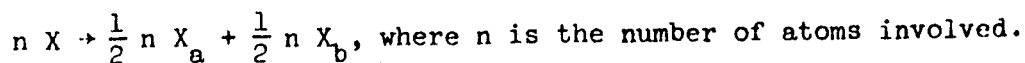
### Introduction

This thesis is concerned with the mechanism of solid solution decomposition in supersaturated tungsten-chromium alloys. The phase diagram for this system is of the type shown in Fig. 1a. The free energy for such a system is known to be of the form shown in Fig. 1b, where the free energy of solution is plotted as a function of composition at three different temperatures. The development of a relative maximum with decreasing temperature is due to the positive enthalpy of mixing for such a system. The relative maximum occurs for temperatures and compositions within the two-phase region. It is possible for an alloy in this region to lower its free energy by an amount  $\Delta G$  (Fig. 1b) to a point on the common tangent to the minima. This common tangent represents the free energy of an alloy having an equilibrium separation of the two phases,  $\alpha_1$ , and  $\alpha_2$ . Consider that an alloy of composition  $X$ , as shown in Figs. 1a and 1b, is homogenized at a temperature ( $t_{ss}$ ) in the single-phase region, then quenched to room temperature to retain the single-phase solid solution. On reheating this alloy at a temperature ( $T_1$ ) in the two-phase region, it has an average driving force  $\Delta G$  to decompose. This paper is concerned with the mechanism of this decomposition.

If we consider small composition fluctuations about the mean solid solution composition,  $X$ , then we can assume that such fluctuations will be equal and opposite, that is,

$$X - X_a = X_b - X, \text{ where } X_a \text{ and } X_b \text{ are shown in Fig. 1b.}$$

The reaction for this fluctuation is



The free energy for the fluctuation  $G_f$  is

$$\Delta G_f = \frac{1}{2} n \left( \frac{G_{X_a}}{N} \right) + \frac{1}{2} n \left( \frac{G_{X_b}}{N} \right) - n \left( \frac{G_X}{N} \right) \quad (1)$$

The quantities in brackets are respectively the free energies per atom of compositions  $X_a$ ,  $X_b$ , and  $X$ . To obtain the free energies per atom of compositions  $X_a$  and  $X_b$ , we can expand the respective free energies in a Taylor series about the point  $X$ , thus:

$$\left( \frac{G_{X_a}}{N} \right) = \frac{1}{N} \left\{ G_X + \left( \frac{\partial G}{\partial X} \right)_X (X_a - X) + \frac{1}{2!} \left( \frac{\partial^2 G}{\partial X^2} \right)_X (X_a - X)^2 + \dots \right\}$$

$$\left( \frac{G_{X_b}}{N} \right) = \frac{1}{N} \left\{ G_X + \left( \frac{\partial G}{\partial X} \right)_X (X_b - X) + \frac{1}{2!} \left( \frac{\partial^2 G}{\partial X^2} \right)_X (X_b - X)^2 + \dots \right\}$$

These terms can be placed into equation (1) to obtain the result:

$$\Delta G_f = \frac{n}{N} \left\{ \frac{1}{2!} \left( \frac{\partial^2 G}{\partial X^2} \right)_X (X_b - X)^2 + \frac{1}{4!} \left( \frac{\partial^4 G}{\partial X^4} \right)_X (X_b - X)^4 + \dots \right\} \quad (2)$$

Using only the second order term,  $\Delta G_f = \frac{n}{2N} \left( \frac{\partial^2 G}{\partial X^2} \right)_X (X_b - X)^2$ , then the stability of the fluctuation is determined by the sign of the second derivative of free energy with respect to composition. The locus of points formed by the second derivative being equal to zero at temperatures within the two-phase region is called the spinodal boundary (shown by dashed lines in Fig. 1c). Alloys having compositions within the spinodal boundary should

decompose with infinitesimal fluctuations and the nucleation should be random or homogeneous. The decomposition process is then one of simple growth as indicated by Fig. 2a.

Alloys within the two-phase region but outside the spinodal boundary cannot decompose with infinitesimal fluctuations because such fluctuations are unstable. In this region of the phase diagram, decomposition must take place by large fluctuations; this gives rise to classical nucleation and growth with the behavior being that shown by Fig. 2b. The incubation time,  $t_0$ , is the time required to form nuclei of the product phases. This process is non-random or heterogeneous, which accounts for the commonly observed grain boundary precipitation in these transformations.

The concept of the spinodal transformations is not a new one, although it has received a great deal of attention in the last few years. According to Borelius,<sup>(1)</sup> Van der Waals was the first one to use the word "spinodal" in conjunction with decomposition processes. Later work by Borelius<sup>(2)</sup> pointed out the significance of the sign of the second derivative of free energy with respect to composition. His studies, which included resistivity measurements on such alloys as Pb-Sn, Au-Pt, Au-Ni, Al-Cu, Al-Zn, pointed to the utility of the second derivative test. X-ray investigations by Bradley<sup>(3)</sup> on copper-nickel-iron alloys decomposed in the two-phase region disclosed the existence of anomalous diffuse "side bands" at small angular distances about the main Bragg lines. These results were explained by Daniel and Lipson<sup>(4)</sup> and Hargreaves.<sup>(5)</sup> They made detailed mathematical analyses of diffraction intensities and postulated that the side bands were caused by the existence of a periodic modulation in lattice parameter and composition, with periods of the order of tens of lattice parameters.

Experimental work by Van der Toorn and Tiedema<sup>(6)</sup> on gold-platinum showed that the modulated structures formed when a solid solution alloy decomposed inside the spinodal region. They solution treated several alloys and decomposed them within the two-phase region, both in and outside the spinodal boundary. Alloys inside the spinodal boundary showed side bands, while alloys outside this region did not. They concluded that the appearance of such side bands was characteristic for alloys undergoing spinodal decomposition. The sequence of events that takes place during decomposition within the spinodal is thought to be:<sup>(7)</sup> Supersaturated Solid Solution → Modulated Matrix Structure → Transition Structure (if any) → Equilibrium structure.

The side bands formed in the modulated stage of decomposition move in towards the main Bragg line on further aging, indicating growth of the wave length of the modulation. Further aging causes the main Bragg line to decrease in intensity. This is followed by the merging of the Bragg line with the side bands, and then the appearance of the transition structure lines, if any, and finally the equilibrium structure lines. Recent theoretical work of Hillert<sup>(8)</sup> and of Cahn<sup>(9)</sup> has shown that alloys inside the spinodal boundary should decompose spontaneously into periodic modulations. These theories also predict a distribution of modulated wave length which accounts for the diffuseness of the side bands. The effect of surface tension and strain energy on the occurrence of the spinodal transformation has been considered by Cahn.<sup>(9)</sup> He concluded that the surface tension would have no effect on the spinodal boundary. The strain energy, however, would have a large effect (in some cases completely suppressing spinodal decomposition, and in all cases increasing the amount

of super-cooling needed).

The use of spinodal transformation as a means for obtaining high strength materials is just now being explored. The maximum yield strength of a material is inversely proportional to the wavelength of the modulations. Since the spinodal decomposition produces very short periods of modulation, it appears that this may be a means for attaining high strength. The results of Van der Toorn and Tiedema<sup>(6)</sup> and of Parker et al.<sup>(10)</sup> on gold-platinum alloys show that large increases in hardness and yield strength do result in such alloys. The increase in both hardness and yield strength was on the order of 300% over the equilibrium two-phase alloys. The yield strength was limited in all cases by grain boundary fracture, and therefore not a true representation of the maximum attainable yield strength for the alloys.

This report describes an investigation of the mechanism of decomposition inside the chemical spinodal of the chromium-tungsten solid solution. It is part of a study relating strength to microstructure. The phase diagram for tungsten-chromium, with chemical spinodal boundary drawn in, is shown in Fig. 3. This phase diagram is based on work by Greenaway<sup>(11)</sup> and was established by x-ray and metallographic means. The spinodal boundary was calculated from the two-phase boundary of the diagram using the method of Cook and Hilliard.<sup>(12)</sup> Tungsten-chromium and molybdenum-chromium<sup>(13)</sup> are the only systems with a simple miscibility gap reported in the literature in which both decomposition phases are body-centered cubic. To date, spinodal decomposition in body-centered cubic systems has not been reported. The lack of information concerning the spinodal decomposition in body-centered cubic systems, along with the possible practical

implications a refractory alloy such as tungsten-chromium might have, prompted the present investigation. The investigation of molybdenum-chromium was ruled out because the top of the miscibility gap is only 900°C and the reaction rates are very slow. Kubaschewski<sup>(13)</sup> reports reaction times on the order of one year for alloys in this system.



### Experimental Procedure

Tungsten-chromium alloys of two different compositions were homogenized in the solid solution region at a temperature of 1750°C for 3 hours. The alloys were then rapidly quenched to room temperature, and reheated to various aging temperatures within the chemical spinodal boundary. The decomposition process was followed by microhardness, x-ray diffraction, and metallographic examinations.

### Materials

The tungsten and chromium used in this experiment were the purest commercially available in the form of powder (-325 mesh). The chromium was supplied by United Mineral and Chemical Corporation, the tungsten by Fansteel Metallurgical. The analysis of the chromium was 99.98% and that of the tungsten was 99.99%.

### Sample Preparation

Alloys of two compositions were prepared. (See Fig. 3 for the location of the alloys within the phase diagram.) Alloy 1 had a composition of 28 atomic% tungsten and 72 atomic % chromium. The composition of alloy 2 was 39 atomic % tungsten and 61 atomic % chromium. These percentages were determined after sintering and solid solution homogenization. The approximate percentages of alloys 1 and 2 were weighed and mixed by tumbling for 3 days in a rotary tumbler. These powders were then compacted in 1/4 inch diameter by 1/4 inch long pellets in a tungsten-carbide die at a pressure of 200,000 psi. The pellets were suspended by a tungsten basket in a vacuum furnace. The furnace was evacuated to  $10^{-6}$  mm Hg and back-filled with purified hydrogen. The hydrogen was purified by passing it over a molecular sieve maintained at liquid nitrogen temperature, then over

titanium-zirconium chips maintained at 800°C. The sample pellets were presintered in the purified hydrogen atmosphere at 1000°C for 24 hours in order to remove most of the surface oxygen. Final sintering and solid solution homogenization was carried out on each sample individually. Each sample was suspended in the furnace evacuated to  $10^{-6}$  mm Hg, and baked out at 700°C for several hours. The furnace was then filled with argon, purified in the way described above for hydrogen, except now using argon boil off, as the melting point of argon is slightly above liquid nitrogen temperature. Sintering and homogenization was carried out in one operation by heating the samples for 3 hours at a temperature of 1750°C. This operation was followed by a rapid quench and then an aging treatment, carried out in two ways. Samples aged at temperatures below 1100°C were sealed in silica glass under a vacuum of  $10^{-6}$  mm Hg and placed in a tube furnace while samples aged at higher temperatures were heated in a vacuum furnace filled with purified argon.

#### Apparatus

A high temperature vacuum quenching furnace was designed for maximum quench rates consistent with the relatively bulky specimens. The main features of this system are shown schematically in Fig. 4. The electrodes and carrying tubes for the quenching media were fed through the walls of the vacuum chamber in a standard manner. All parts on the vacuum side of the vacuum gate valve (G, Fig. 4) and parts inside the vacuum chamber were designed to be taken out of the system. These parts could then be washed along with the inside of the furnace after each run. After washing with trichlorethylene these items were rinsed in acetone, followed by isopropyl alcohol, and baked out at a temperature of 150°C for 6 hours under a vacuum of  $10^{-6}$  mm Hg to insure cleanliness.

Several heating and quenching schemes were tried. The one described here gave the most consistently good results. A sample was suspended by a tungsten wire basket from the top quenching nozzle into the center of the heating filament. This filament was constructed of 0.003" tantalum foil in the form of an almost closed cylinder 1/2 in. diameter by 1-1/2 in. high. The heating power was supplied by a 0-500 amp, 0-20v, constant voltage, constant current power supply. Distilled water atomized into a high velocity stream of helium was found to give high quenching rates and a minimum of surface contamination (removed by grinding). The control of the quenching cycle proved to be an important issue in determining the effective quenching rate. To increase consistency in the heating - quench cycle, an electronic control cycle timer was employed. The electronic timer was set so that at the end of the 3 hour sintering-homogenization cycle employed, it would trigger power to three circuits--the first circuit being the solenoid operated water valve which opens at this time, and the second and third circuits being series arranged time delays. These time delay circuits were simple variable resistance R-C triggered solid-state devices. After the water valve was opened there was a delay of approximately 300 milliseconds for the water to reach the atomizing nozzle before the vacuum gate valve was opened. Then there was a delay of 40 milliseconds for the helium-water mixture to reach the specimen before the power was turned off. The latter time delay was needed because without it the temperature would fall a significant amount, due to radiation losses, before the main quench began. A capacitor discharge was needed to supply the initial surge of current to the vacuum solenoid valve. Otherwise it would not open consistently. Typical quenching curves are shown in Fig. 5. These pictures were taken on a Tektronix 502 dual-beam oscilloscope. The

oscilloscope was triggered at the same time that the vacuum valve was opened. The upper beam represents temperature as measured by 0.005 in. Pt/Pt + 10% Rh thermocouple wires mounted across from each other on the diameter of the specimen. The lower beam represents the furnace power. It should be noted in Fig. 5b that the full wave rectified signal (lower beam) dies out after the start of the quench.

Temperatures were measured with a "Pyro Micro-optical Pyrometer". This instrument was calibrated by comparing the temperature measured to temperature given by a thermocouple attached to the specimen. This calibration was extrapolated beyond temperatures of 1600°C due to the lack of accurate thermocouples in this range.

#### Techniques

After quenching, the samples were ground and polished. The grain size of the sample was small enough so that x-ray diffraction investigations could be carried out on the bulk samples in a diffractometer. Two diffractometer runs were made on each sample after each aging treatment. One of the traces was run on the sample surface as it came out the furnace or quartz glass capsule, and one on a freshly prepared surface. All diffraction experiments were carried out using Cu K $\alpha$  radiation. The diffractometer was standardized for line position and intensity after each experimental run.

An electron beam microprobe was used in conjunction with metallography to identify phases in the early stages of precipitation. Specimens were prepared for metallography by polishing with chrome-oxide and etching electrolytically. The specimens were etched for 30 sec. in a solution of 2 g NaOH, 20 ml H<sub>2</sub>O, and 50 ml glycerin, using a potential of 20v.

Metallography

Metallography confirmed the x-ray results, indicating that the decomposition process is one of nucleation and growth. This is shown by micrographs of the aging sequence, for alloy 1, in Figs. 11 to 18 and the completely decomposed alloy in Fig. 19. The new phase, identified by an electron beam microprobe to be the tungsten rich decomposition phase, is seen to grow out of the grain boundaries. A representative micrograph of alloy 2 in the completely decomposed condition is shown in Fig. 20.

Discussion

Alloys that decompose by a spinodal mechanism possess three main characteristic features: 1- existence of x-ray side bands in the early stages of decomposition, 2- simple growth characteristics, 3- random precipitation. None of these features characterizing the spinodal transformation exist in the decomposition of tungsten-chromium alloys. There is no x-ray evidence of the existence of side bands. The time-transformation curves, in Figs. 6 to 8, show that the decomposition process is not one of simple growth, but rather one of nucleation and growth. The precipitation is not random as in the case of an ideal spinodal decomposition, but rather it is concentrated at the grain boundaries as shown in Figs. 11 to 16. This x-ray and metallographic evidence shows that the decomposition process in the tungsten-chromium system does not occur by a spinodal mechanism. This conclusion is in agreement with Cahn's<sup>(9)</sup> theory of spinodal decomposition. Cahn has calculated the amount of supercooling necessary for spinodal decomposition, taking into account strain energy. He concluded that for an alloy of critical composition (i.e. an alloy at the top of the miscibility gap):

$$T_c - T = \frac{\eta^2 E}{2 (1-\nu) k N_v}$$

where

- $T_c$  = critical temperature (top of miscibility gap),
- $\eta$  = linear expansion per unit composition change,
- $E$  = Young's modulus,
- $\nu$  = Poisson's ratio

$k$  = Boltzmann's constant,

$N_v$  = number of atoms per unit volume.

Table II below shows that when  $\eta$  is small, the required amount of supercooling is experimentally attainable and spinodal decomposition is observed.

Table II

The Occurrence of Spinodal Decomposition  
With Respect to the Parameter

<u>System</u>	<u>Crystal Lattice</u>	<u><math>\eta</math></u>	<u><math>T - T_c</math> °C</u>	<u>Spinodal</u>
Al-Zn	FCC	0.0257	40	YES
Au-Pt	FCC	0.038	200	YES
Cr-W	BCC	0.093	1900	NO
Au-Ni	FCC	0.150	2000	NO

The strain energy term is seen to be an important factor in determining the mechanism of decomposition within the chemical spinodal boundary.

The microstructure of alloy 1 in the later stages of decomposition is shown in Figs. 16 to 19. This microstructure resembles that of lamellar pearlite, such as is found in the iron-carbon system. Earlier work on the tungsten-chromium system<sup>(11)</sup> also disclosed the eutectoid or pearlitic nature of the microstructure. It is reasonable that a pearlitic microstructure should develop in a miscibility gap system, because such a system represents a simple, unsuppressed eutectoid. Spencer and Mack<sup>(14)</sup> have

observed that a common feature of systems developing a pearlitic microstructure is the shift of the Bragg lines, for the decomposition phases, on aging. The shift, which is away from the solid solution line, was observed in the present work, thus indicating that the decomposition of tungsten-chromium alloys might follow the mechanism of decomposition characteristic of the pearlite reaction.



### Summary and Conclusions

The mechanism of solid solution decomposition within the chemical spinodal boundary has been investigated for the tungsten-chromium system. X-ray and metallographic evidence indicate that the decomposition process is one of nucleation and growth. This is evidence of the importance of the strain energy term in determining the mechanism of decomposition within the chemical spinodal, and is in accord with Cahn's<sup>(9)</sup> theory for the occurrence of spinodal decomposition. The decomposition of tungsten-chromium solid solution occurs by the "pearlite" mechanism.

The activation energy for the decomposition process was measured to be 57.5 Kcal per mole. This is less than the activation energies for self diffusion in tungsten (136 Kcal/mole), or chromium (73.2 Kcal/mole).<sup>(15)</sup> However, it is difficult to obtain meaningful activation energy values in nucleation and growth processes because these two processes are controlled by different factors and they interact in a complex manner.

Microhardness studies reveal that tungsten-chromium alloys attain high hardness during the early stages of aging, despite the early loss of coherency.

Acknowledgments

The author wishes to acknowledge the advice and encouragement of Professor E. R. Parker and Dr. V. F. Zackay.

This work was done under the auspices of the U.S. Atomic Energy Commission through the Inorganic Materials Research Division of the Lawrence Radiation Laboratory.

References

1. Citation made by G. Borelius (no Reference to Van der Waals)  
Trans. AIME, p. 477, June, 1951.
2. G. Borelius, Ann. Physik Lpz., 20, 57 (1934).  
Ann. Physik Lpz., 24, 489 (1935).  
Ann. Physik Lpz., 28, 507 (1937).  
Ann. Physik Lpz., 33, 517 (1938).  
Ark. Mat. Astr. Fys. 32A, No. 1 (1945).  
G. Borelius, P. Larris, and E. Ohlson, Ark. Mat. Astr. Fys., 31A,  
No. 10, (1944).
3. A. J. Bradley, Proc. Phys. Soc. (London), 52, 80 (1940).
4. V. Daniels and H. Lipson, Proc. Roy. Soc. (London) (A) 181, 368 (1943).  
V. Daniels and H. Lipson, Proc. Roy. Soc. (London) (A) 182, 378 (1944).  
V. Daniels and H. Lipson, Proc. Roy. Soc. (London) (A) 192, 575 (1948).
5. M. E. Hargreaves, Acta Cryst., 2, 259 (1949).  
M. E. Hargreaves, Acta Cryst., 4, 301 (1951).
6. L. J. Van der Toorn and T. J. Tiedema, Acta Met., 8, 711 (1960).  
L. J. Van der Toorn and T. J. Tiedema, Acta Met., 8, 715 (1960).
7. J. Mauenc, Rev. Met., 54, 867 (1957).  
C. Buckle, B. Gentry, and J. Mauenc, Rev. Met., 56, 247 (1959).  
J. Mauenc, Acta Cryst., 10, 259 (1957).  
J. Mauenc, Acta Met., 7, 124 (1959).
8. M. Hillert, Acta Met., 9, 525 (1961).
9. J. W. Cahn, Acta Met., 9, 795 (1961).  
J. W. Cahn, Acta. Met., 10, 179 (1962).
10. E. R. Parker, R. W. Carpenter, and V. F. Zackay, International Conf. on  
Fracture, Sendai, Japan (1965). (In Press)

11. H. T. Greenawa, J. Inst. Metals 80, 589 (1951-52).
12. H. E. Cook and J. E. Hilliard, Trans. AIME, 233, 142 (1965).
13. O. Kubaschewski and T. G. Chart, J. Inst. Metals, 93, 329 (1964-65).
14. C. W. Spencer and D. J. Mack, Decomposition of Austenite by Diffusional Processes, Ed. by V. F. Zackay and H. I. Aaronson, Interscience Publishers, New York, p. 549 (1962).
15. D. Lazarus, Conference. Diffusion in Body-Centered Cubic Materials, Gatlinberg, Tennessee, 1964. (In press)

FIGURE CAPTIONS

Fig. 1a Phase diagram for binary alloy system with simple miscibility gap.

Fig. 1b Free energy as a function of composition for the solid portion of the system shown in Fig. 1a, at three different temperatures.

Fig. 1c Phase diagram with spinodal boundaries drawn in.

Fig. 2a Time-transformation curves for simple growth, at two different temperatures.

Fig. 2b Time-transformation curves for nucleation and growth, at two different temperatures.

Fig. 3 Phase diagram for the tungsten-chromium system with the chemical spinodal boundaries drawn in.

Fig. 4 Schematic view of heating-quenching apparatus.

Legend: A - high current, water-cooled power leads

B - water-cooled heating filament clamp

C - electrical insulation

D - specimen

E - refractory metal heating filament

F - carrying tubes for quenching media

G - solenoid-operated vacuum gate valve

H - atomizing nozzle

I - needle-valve for control of water flow

J - solenoid valve

K - container holding distilled water under gas pressure

L - large surge tank

Fig. 5a Typical quenching curve for a static argon quench.

Upper beam: temperature - 200°C/div

Lower beam: furnace power - 5v/div

Time scale: 5sec/div

Quench rate  $\left(\frac{\partial T}{\partial t}\right)$ : ~400°C/sec

Fig. 5b Typical quenching curve for a helium-water, dynamic quench

Upper beam: temperature - 200°C/div

Lower beam: furnace power - 5v/div

Time scale: 20 m sec/div

Quench rate  $\left(\frac{\partial T}{\partial t}\right)$ : ~20,000° C/sec

Fig. 6 Time-transformation curve for 900°C.

Fig. 7 Time-transformation curve for 1100°C.

Fig. 8 Time-transformation curve for 1300°C.

Fig. 9 Logarithm of the time to half transformation plotted against the reciprocal of the absolute temperature.

Fig. 10a Vickers hardness as a function of time at 700, 1100, and 1300°C.

The coefficient of variation is given with each experimental point.

Fig. 10b The ratio of the increase in hardness at a given time to the maximum increase in hardness, for temperatures 700, 1100, and 1300°C.

Fig. 11 Typical micrograph of alloy 1 in the solution-treated and quenched condition.

Fig. 12 Micrograph of alloy 1 as solution-treated, quenched, and aged for 10 min. at 1100°C.

Fig. 13 Micrograph of alloy 1 as solution-treated, quenched, and aged for 20 min. at 1100°C.

Fig. 14 Micrograph of alloy 1 as solution-treated, quenched, and aged for 43 min. at 1100°C.

Fig. 15 Micrograph of alloy 1 as solution-treated, quenched, and aged for 118 min. at 1100°C.

Fig. 16 Micrographs of alloy 1 as solution-treated, quenched, and aged a) b) for 817 min. at 1100°C.

Fig. 17 Micrograph of alloy 1 as solution-treated, quenched, and aged for 3912 min. at 1100°C.

Fig. 18 Micrograph of alloy 1 as solution-treated, quenched, and aged a) b) c) for 10,332 min. at 1100°C.

Fig. 19 Micrograph of alloy 1 as solution-treated, quenched, and aged a) b) for 920 min. at 1300°C.

Fig. 20 Micrograph of alloy 2 as solution-treated, quenched, and aged for 2000 min. at 1000°C.

Fig. 1a

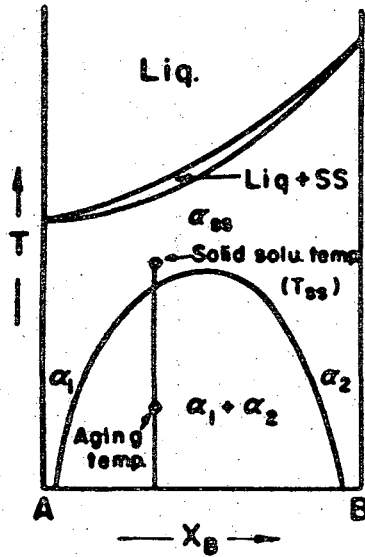


Fig. 1b

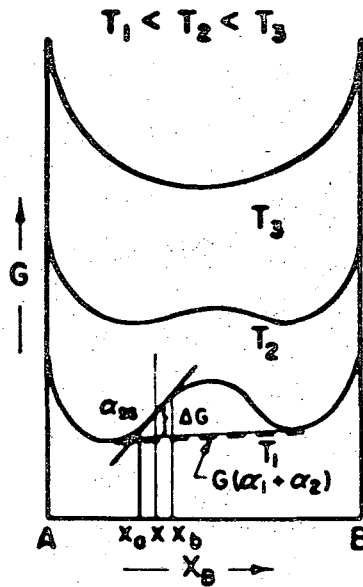


Fig. 1c

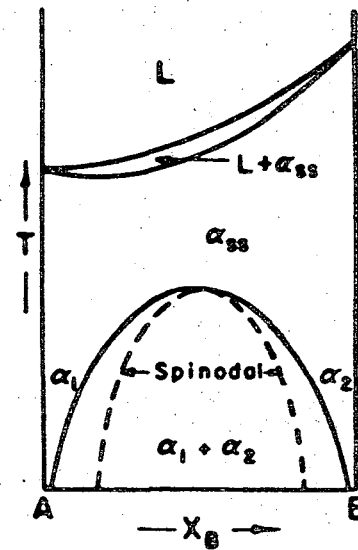


Figure 1a. Phase diagram for binary alloy system with simple miscibility gap.

Figure 1b. Free energy as a function of composition for the solid portion of the system shown in Fig. 1a, at three different temperatures.

Figure 1c. Phase diagram with spinodal boundaries drawn in.



Fig. 2a

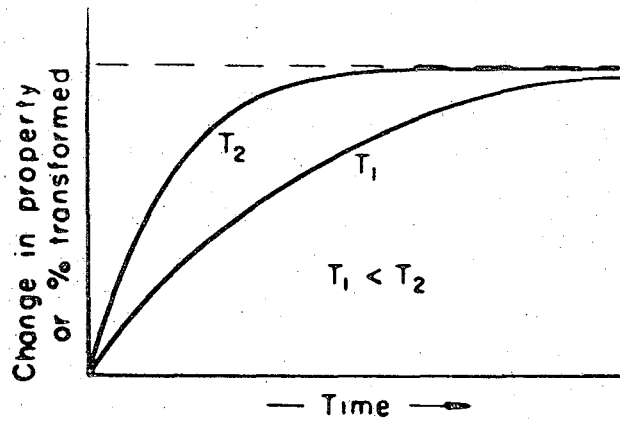


Fig 2b

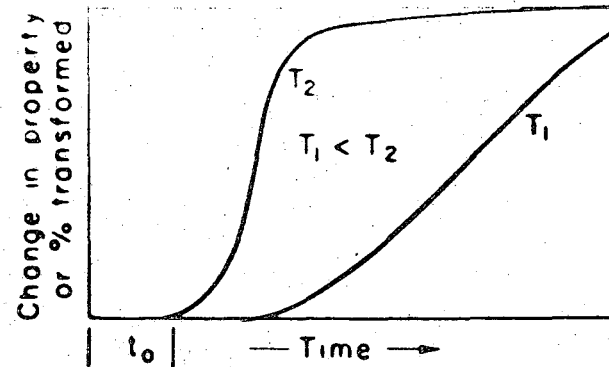


Figure 2a. Time-transformation curves for simple growth, at two different temperatures.

Figure 2b. Time-transformation curves for nucleation and growth, at two different temperatures.

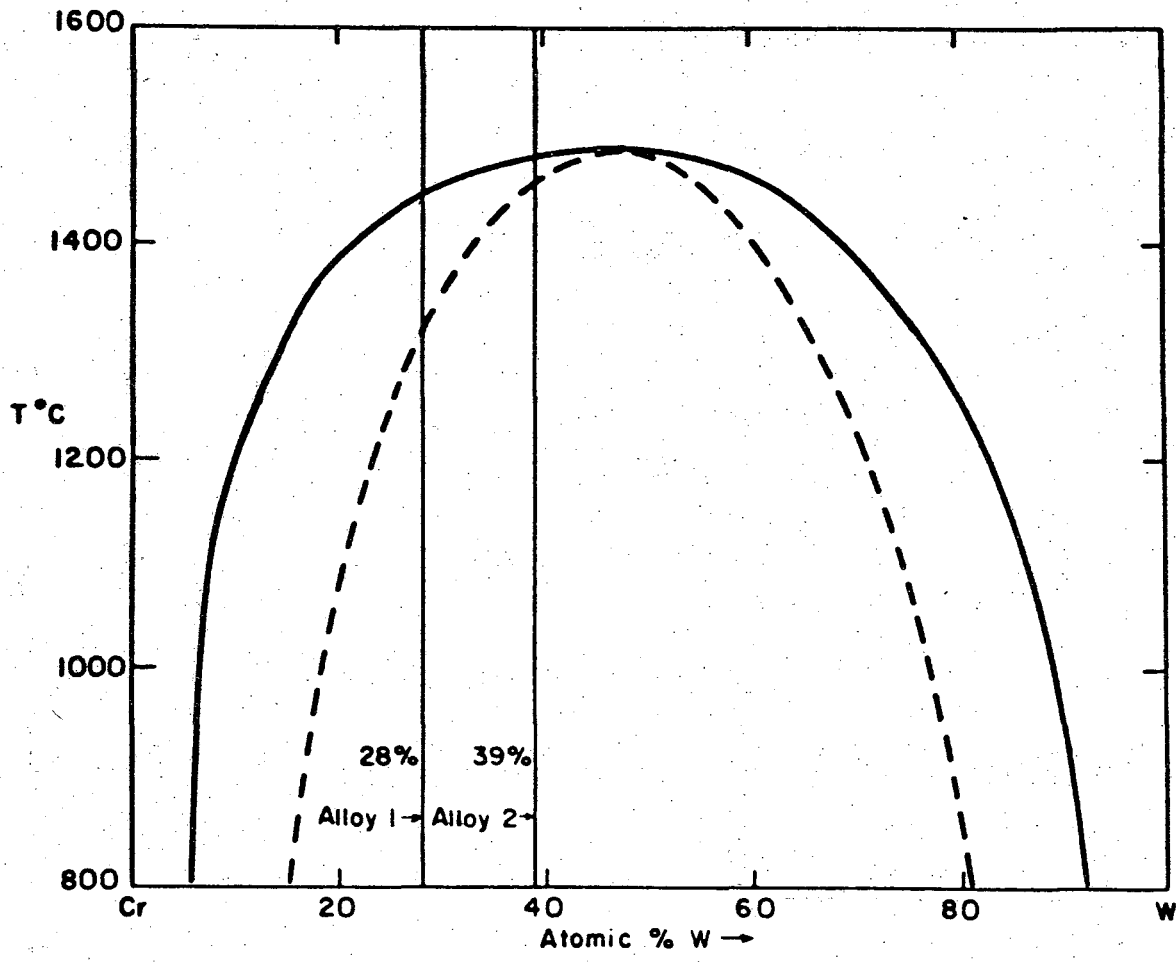
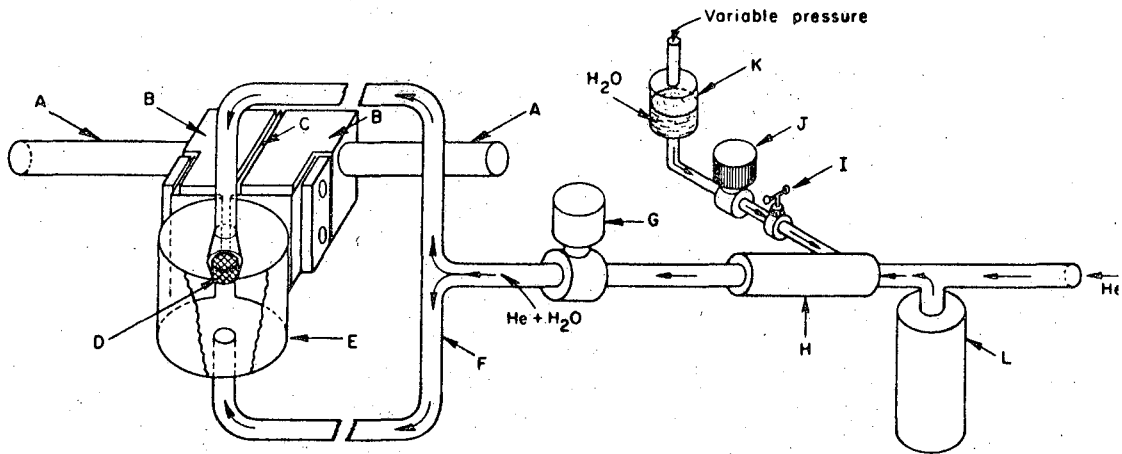


Figure 3. Phase diagram for the tungsten-chromium system with the chemical spinodal boundaries drawn in.



MU 37119

Figure 4. Schematic view of heating-quenching apparatus.

- Legend:
- A - high current, water-cooled power leads
  - B - water-cooled heating filament clamp
  - C - electrical insulation
  - D - specimen
  - E - refractory metal heating filament
  - F - carrying tubes for quenching media
  - G - solenoid-operated vacuum gate valve
  - H - atomizing nozzle
  - I - needle-valve for control of water flow
  - J - solenoid valve
  - K - container holding distilled water under gas pressure
  - L - large surge tank

Fig. 5a

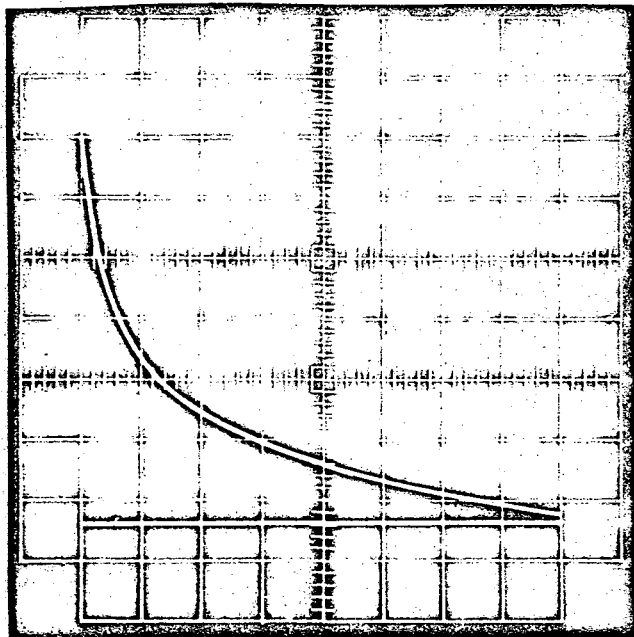


Figure 5a. Typical quenching curve for a static argon quench.

Upper beam: temperature -  $200^{\circ}\text{C}/\text{div}$   
Lower beam: furnace power -  $5\text{v}/\text{div}$   
Time scale:  $5\text{sec}/\text{div}$   
Quench rate  $(\frac{\partial T}{\partial t})$ :  $\sim 400^{\circ}\text{C}/\text{sec}$

Fig. 5b

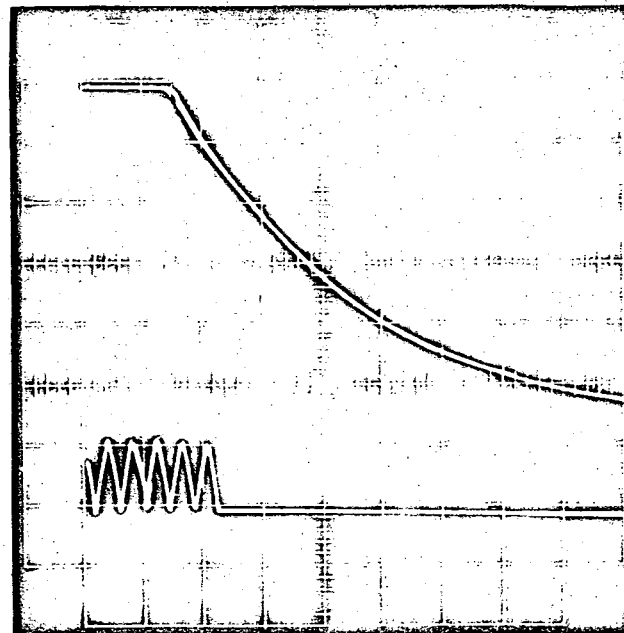


Figure 5b. Typical quenching curve for a helium-water, dynamic quench.

Upper beam: temperature -  $200^{\circ}\text{C}/\text{div}$   
Lower beam: furnace power -  $5\text{v}/\text{div}$   
Time scale:  $20\text{ m sec}/\text{div}$   
Quench rate  $(\frac{\partial T}{\partial t})$ :  $\sim 20,000^{\circ}\text{C}/\text{sec}$

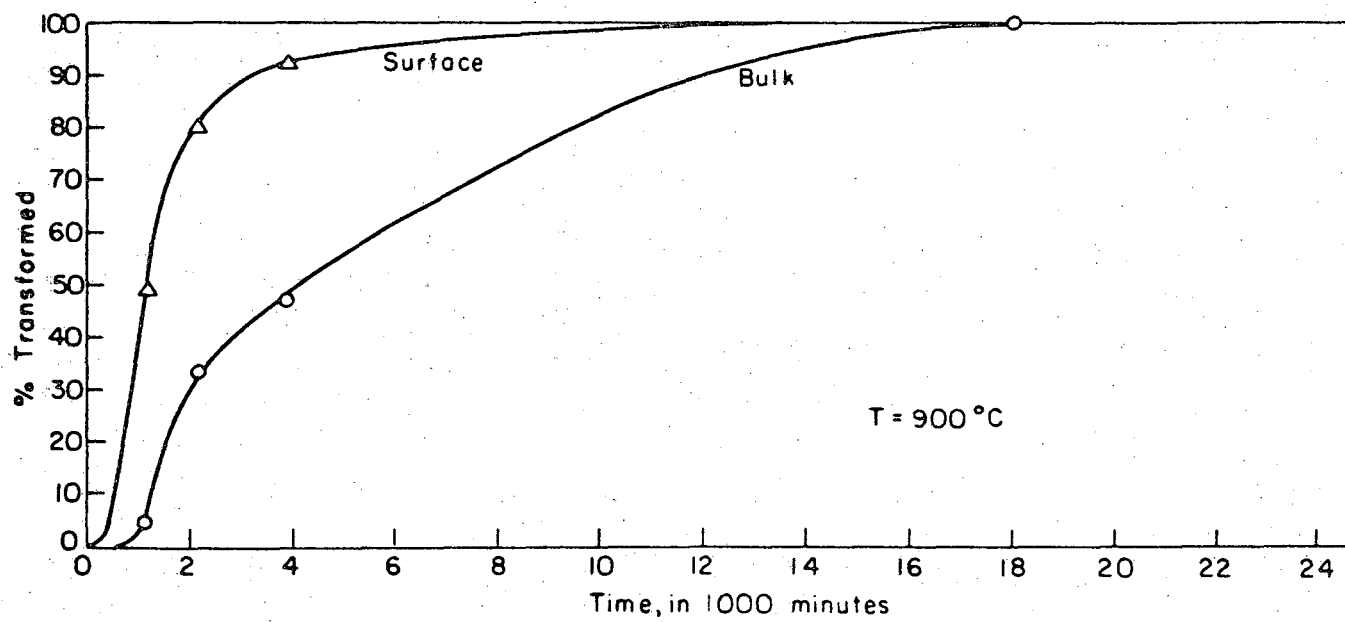


Figure 6. Time-transformation curve for 900°C.

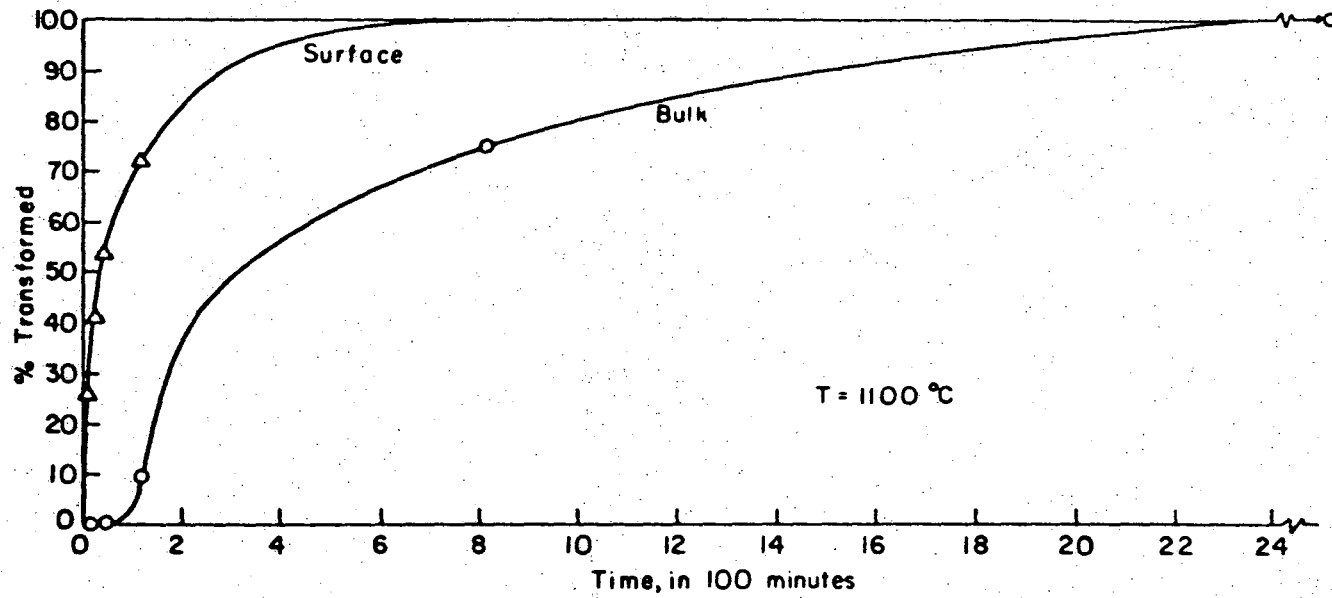


Figure 7. Time-transformation curve for 1100°C.

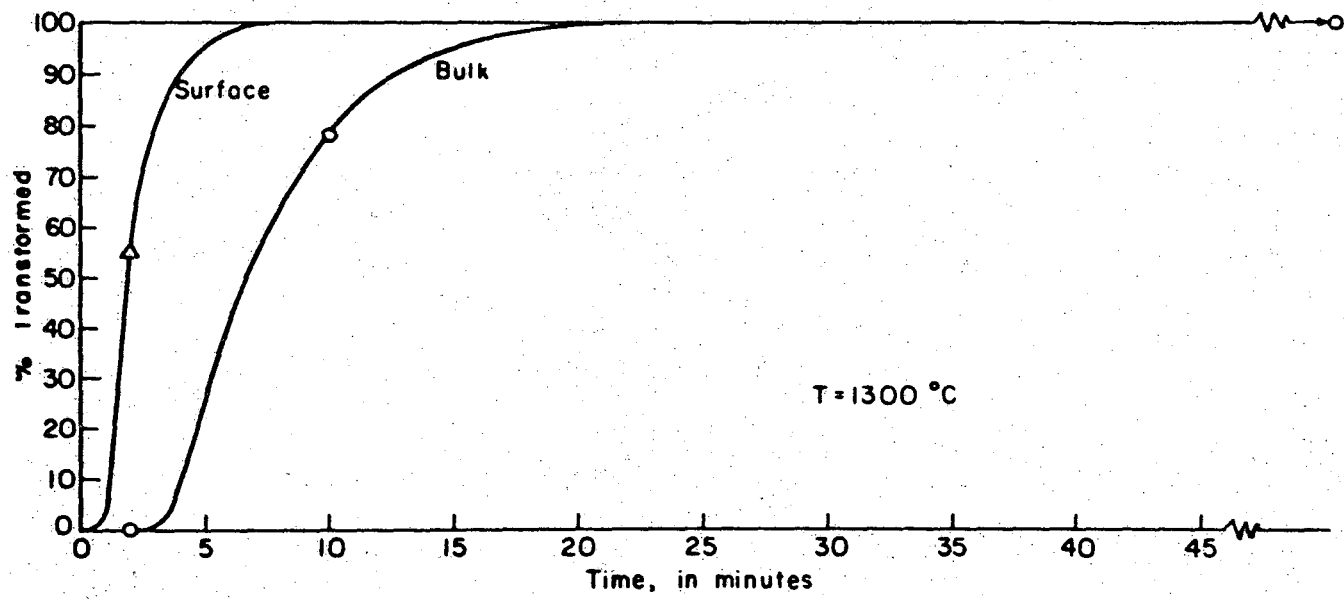


Figure 8. Time-transformation curve for 1300°C.

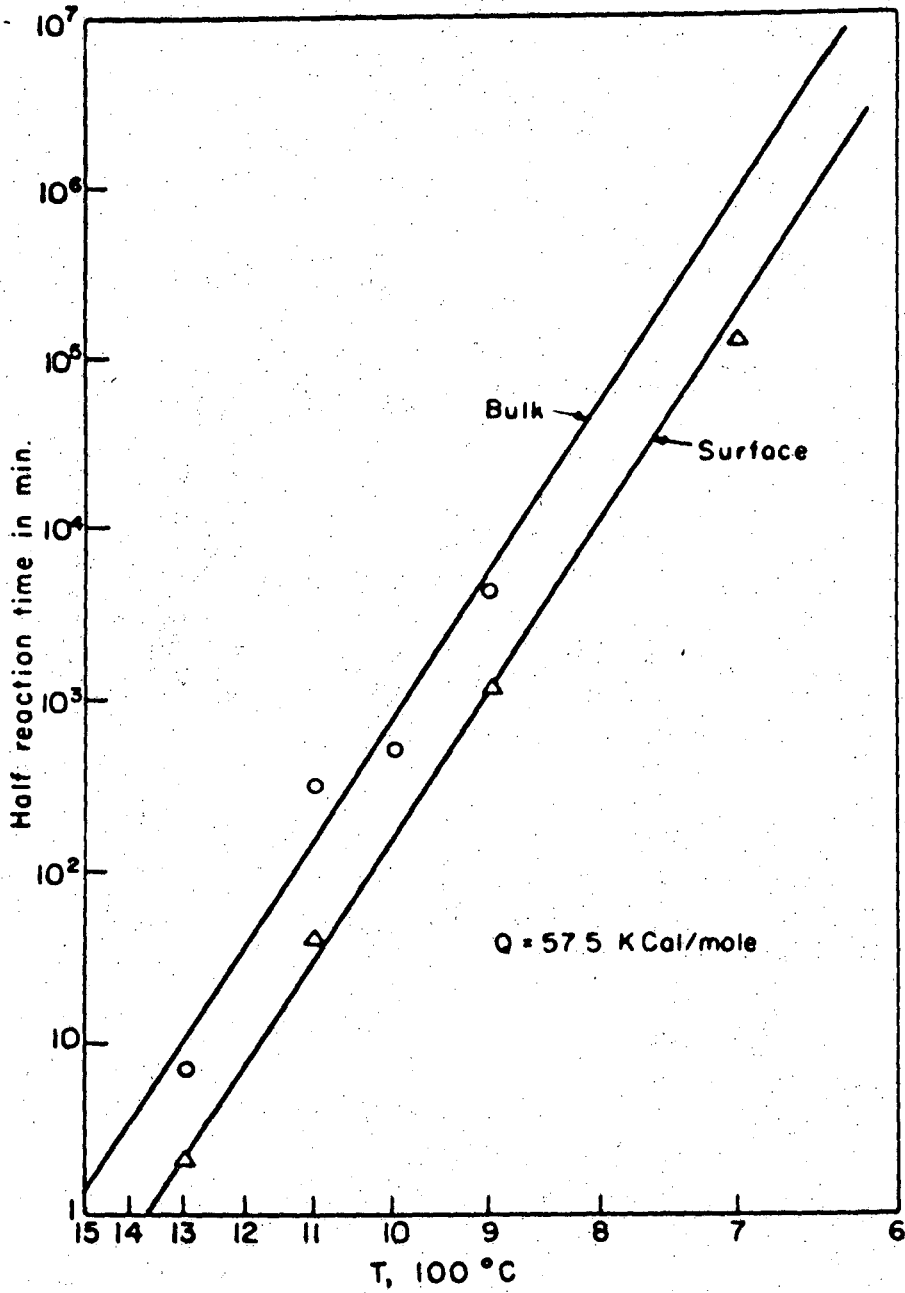


Figure 9. Logrithm of the time to half transformation plotted against the reciprocal of the absolute temperature.



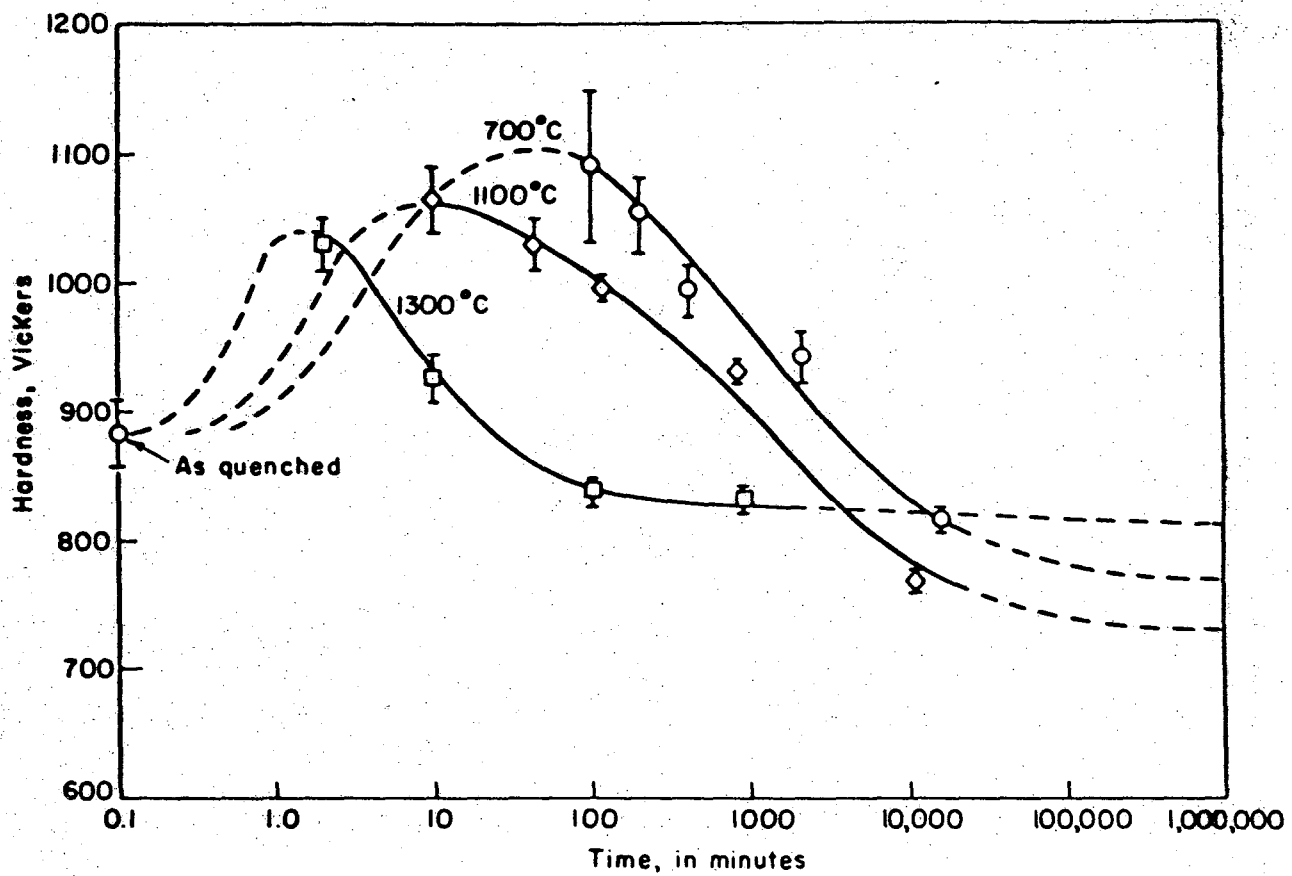


Figure 10a. Vickers hardness as a function of time at 700, 1100, and 1300°C. The coefficient of variation is given with each experimental point.

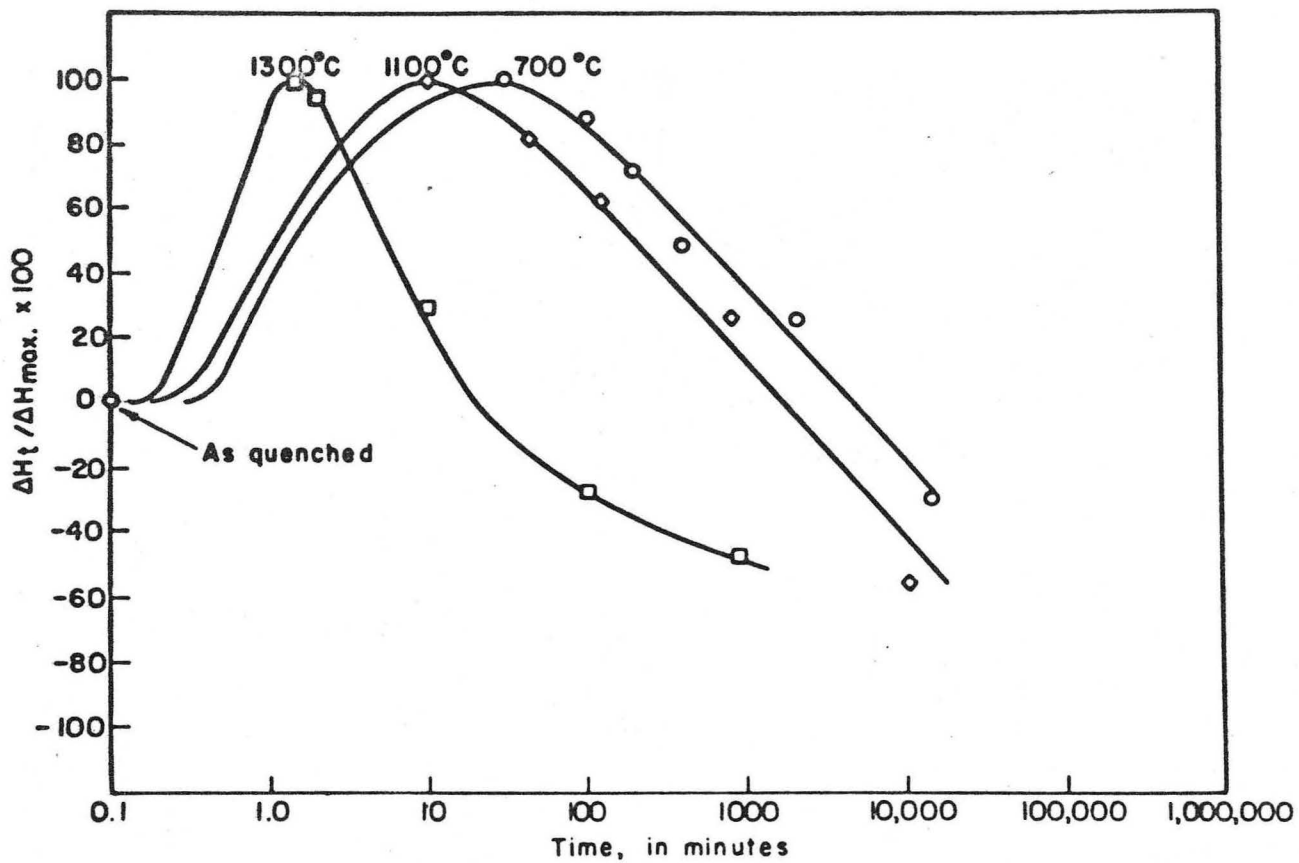
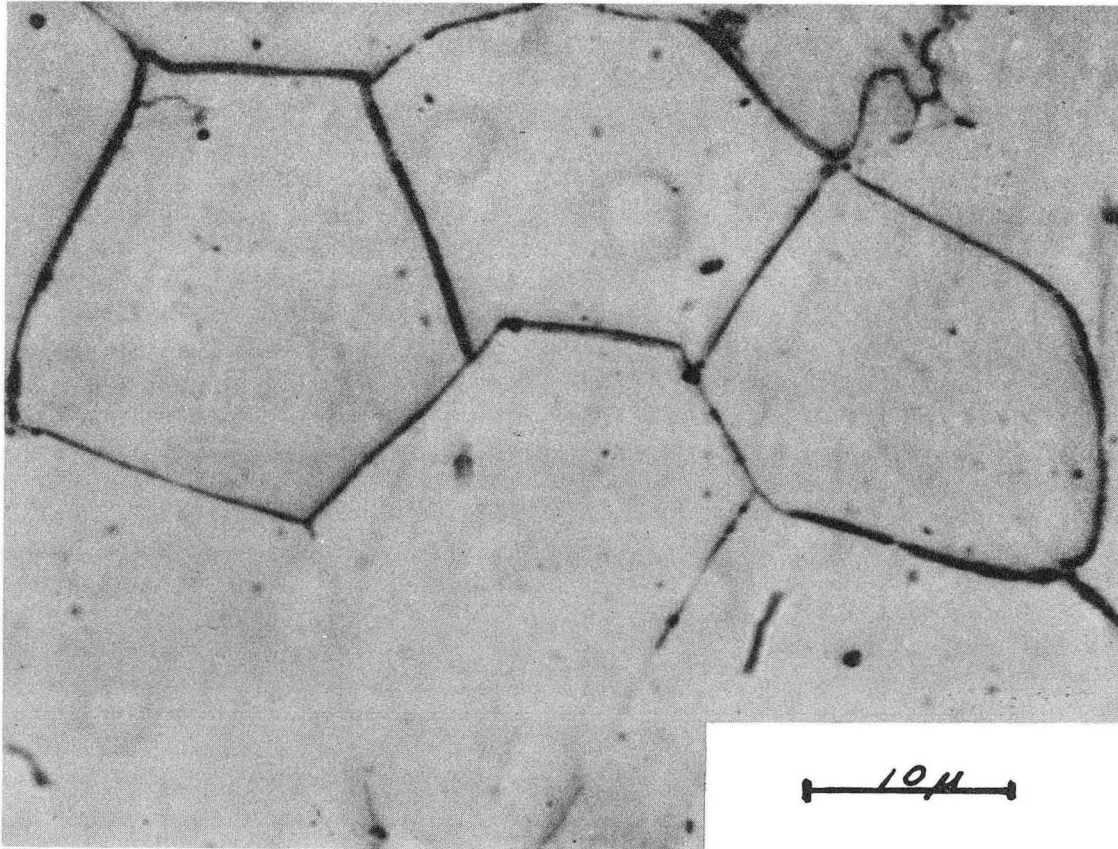
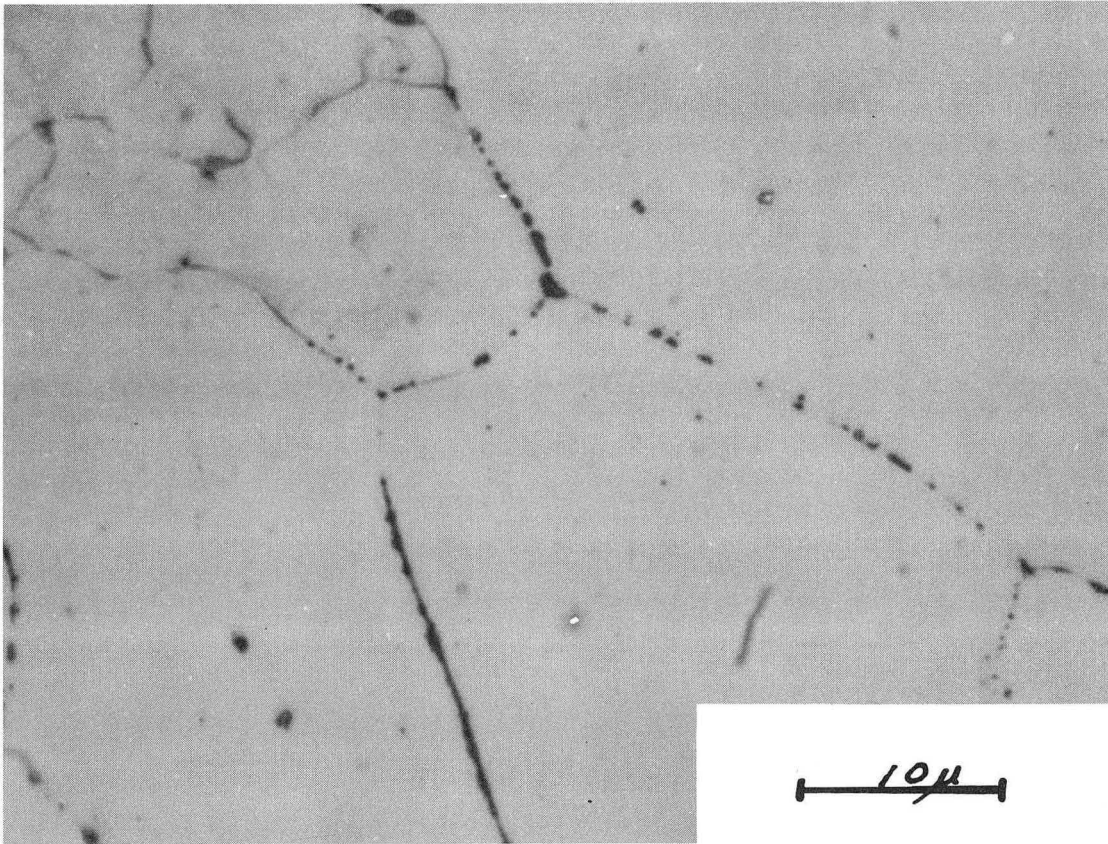


Figure 10b. The ratio of the increase in hardness at a given time to the maximum increase in hardness, for temperatures 700, 1100, and 1300°C.



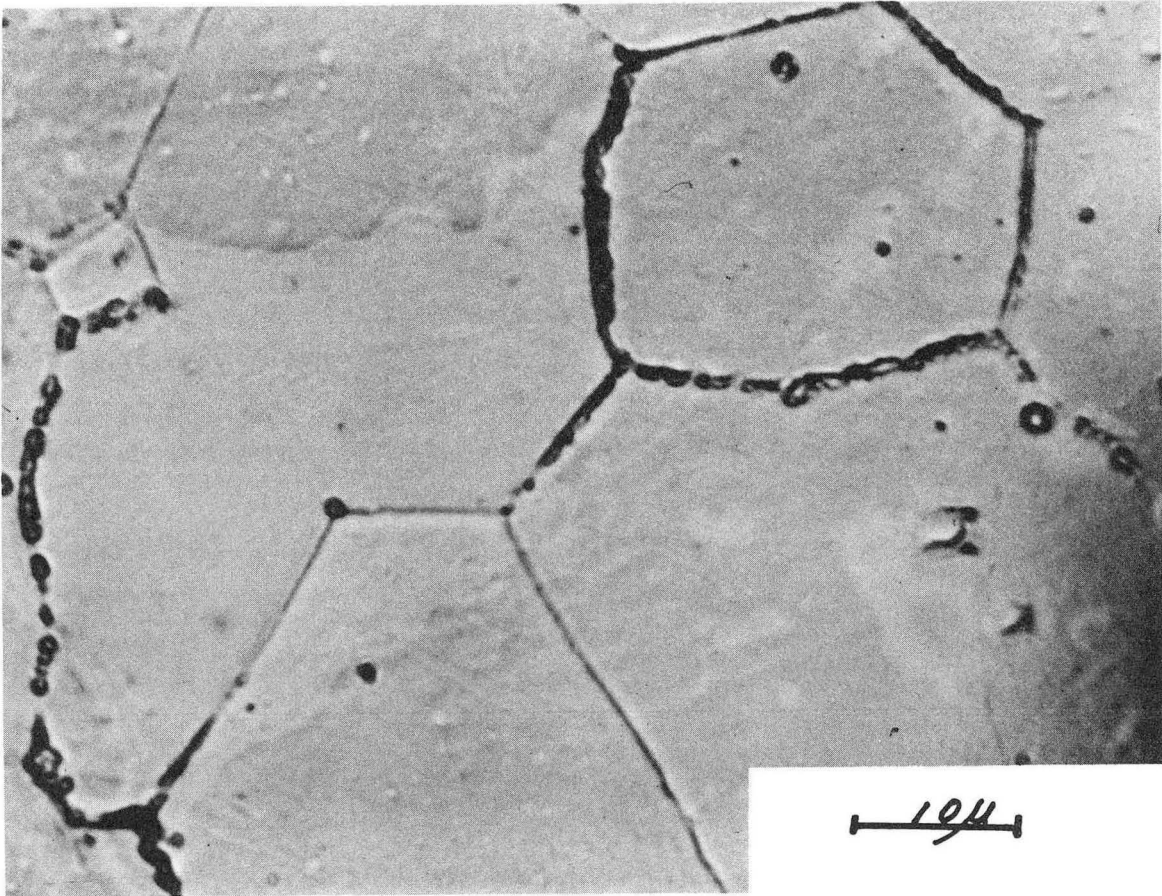
ZN-5614

Fig. 11 Typical micrograph of alloy 1 in the solution-treated and quenched condition.



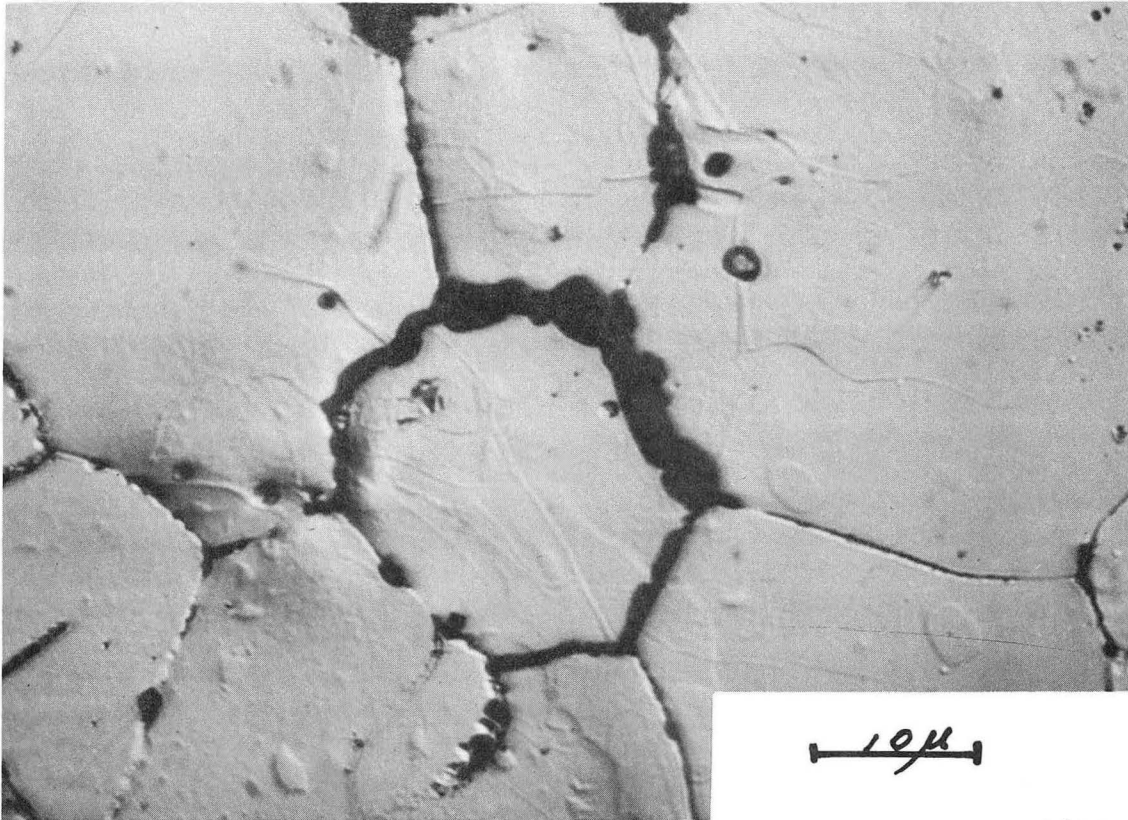
ZN-5669

Fig. 12 Micrograph of alloy 1 as solution-treated, quenched, and aged for 10 min. at 1100°C.



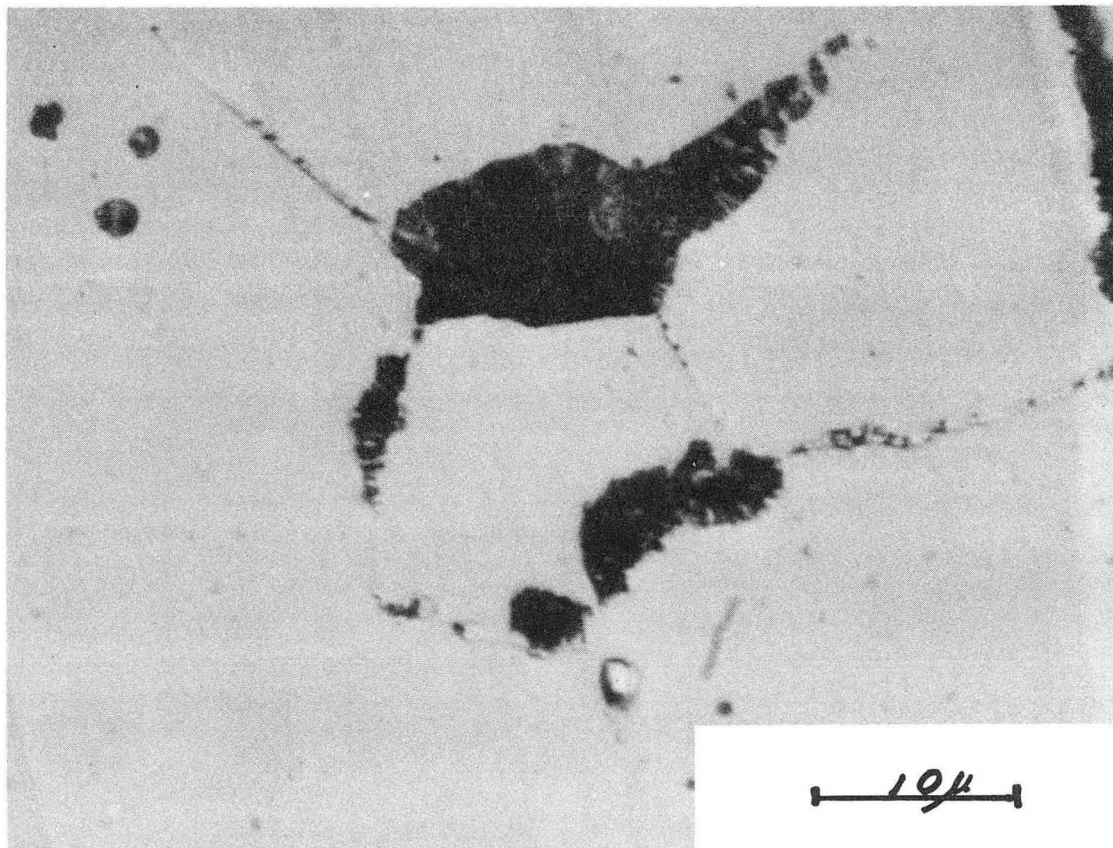
ZN-5616

Fig. 13 Micrograph of alloy 1 as solution-treated, quenched, and aged for 20 min. at 1100°C.



ZN-5615

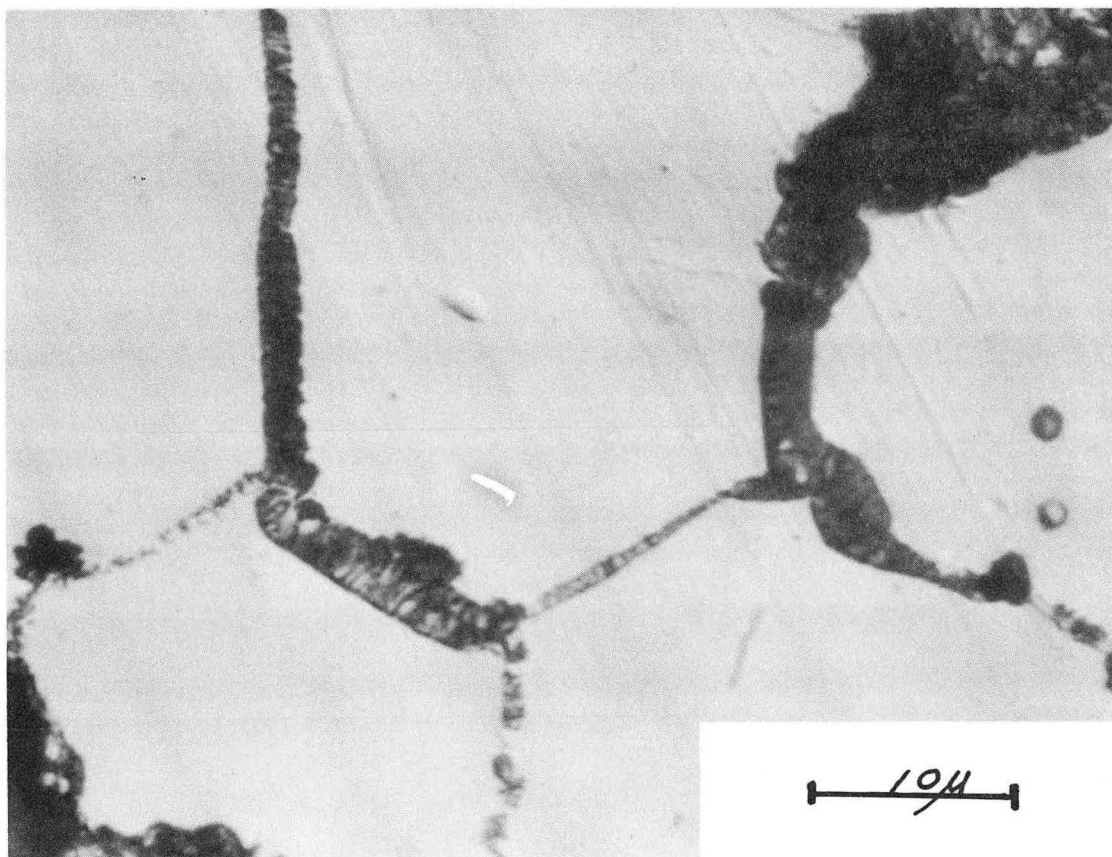
Fig. 14 Micrograph of alloy 1 as solution-treated, quenched, and aged for 43 min. at 1100°C.



ZN-5613

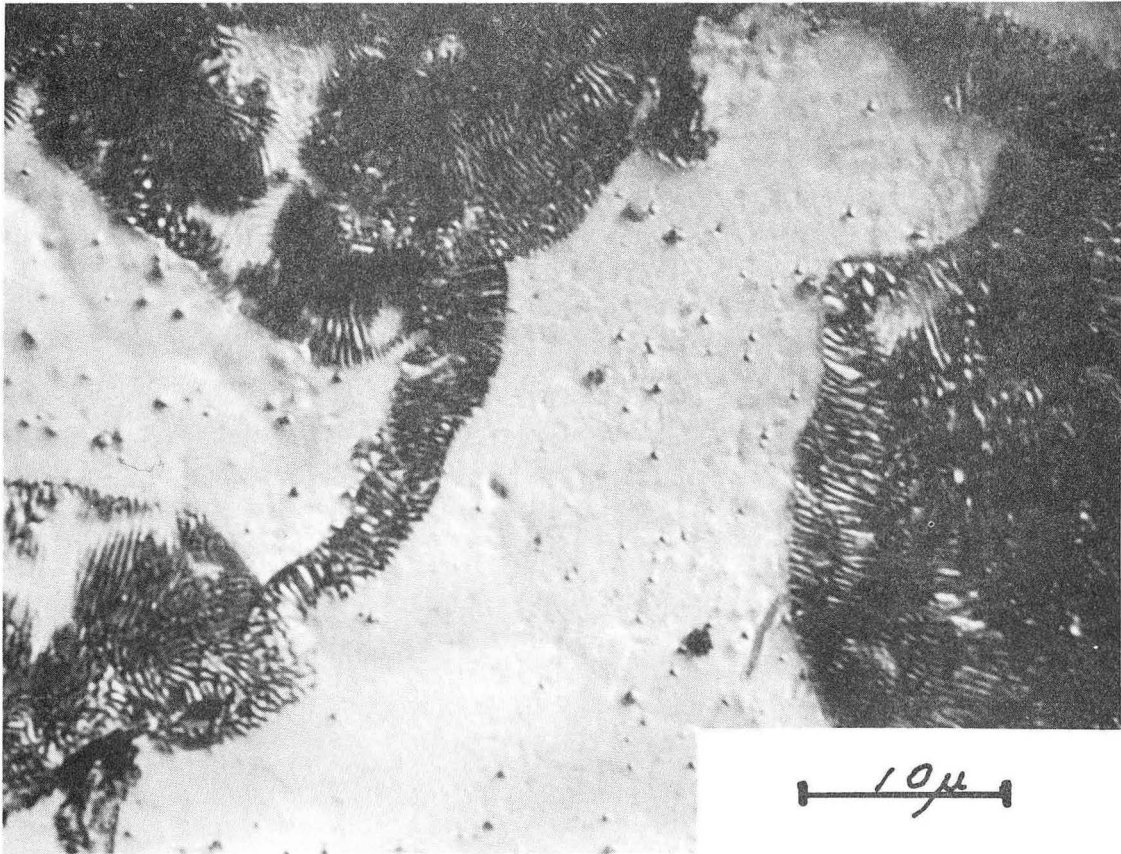
Fig. 15 Micrograph of alloy 1 as solution-treated, quenched, and aged for 118 min. at 1100°C.





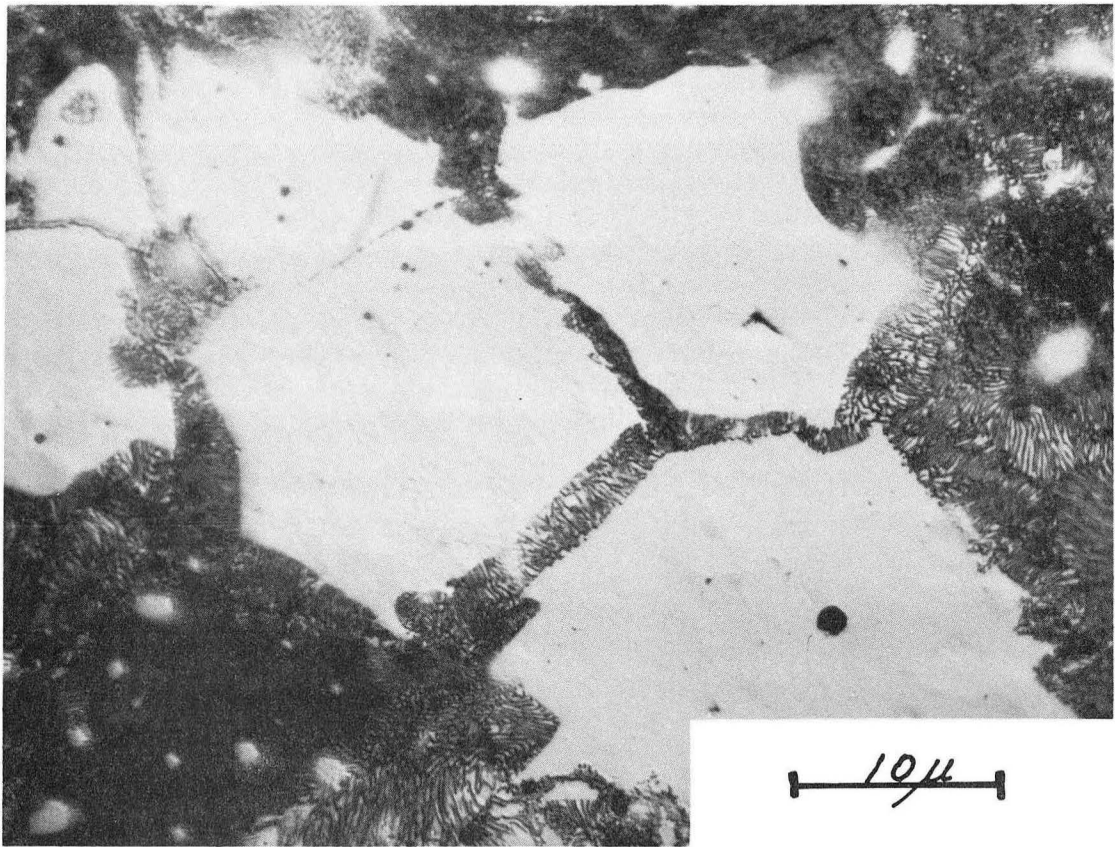
ZN-5620



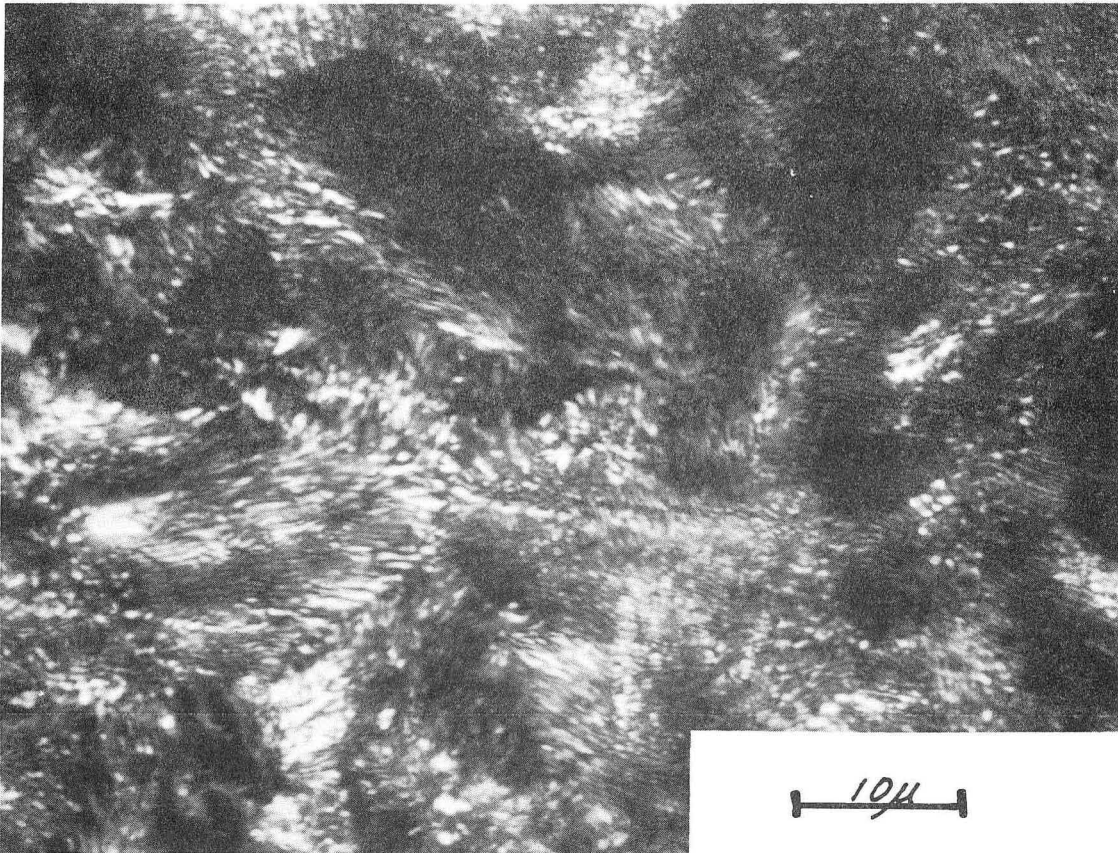


ZN-5667

Fig. 16 Micrographs of alloy 1 as solution-treated, quenched, and  
a) b)  
for 817 min. at 1100°C.

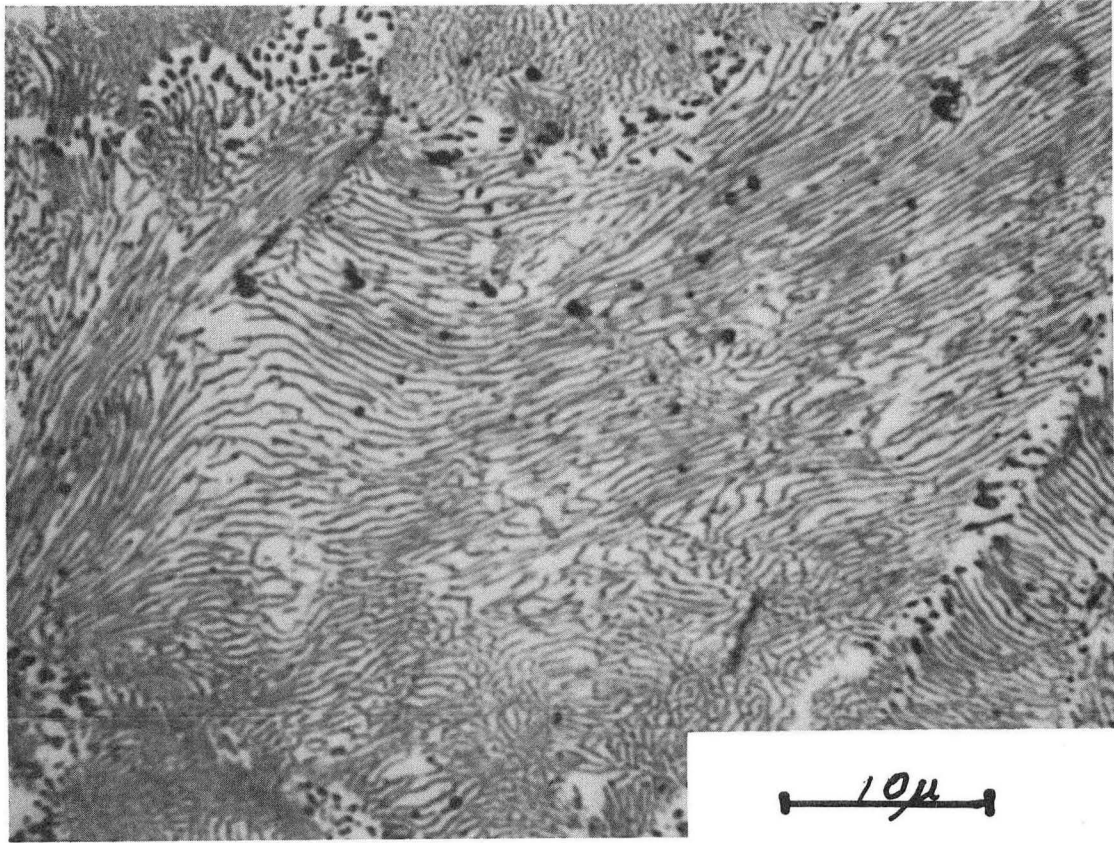


ZN-5622



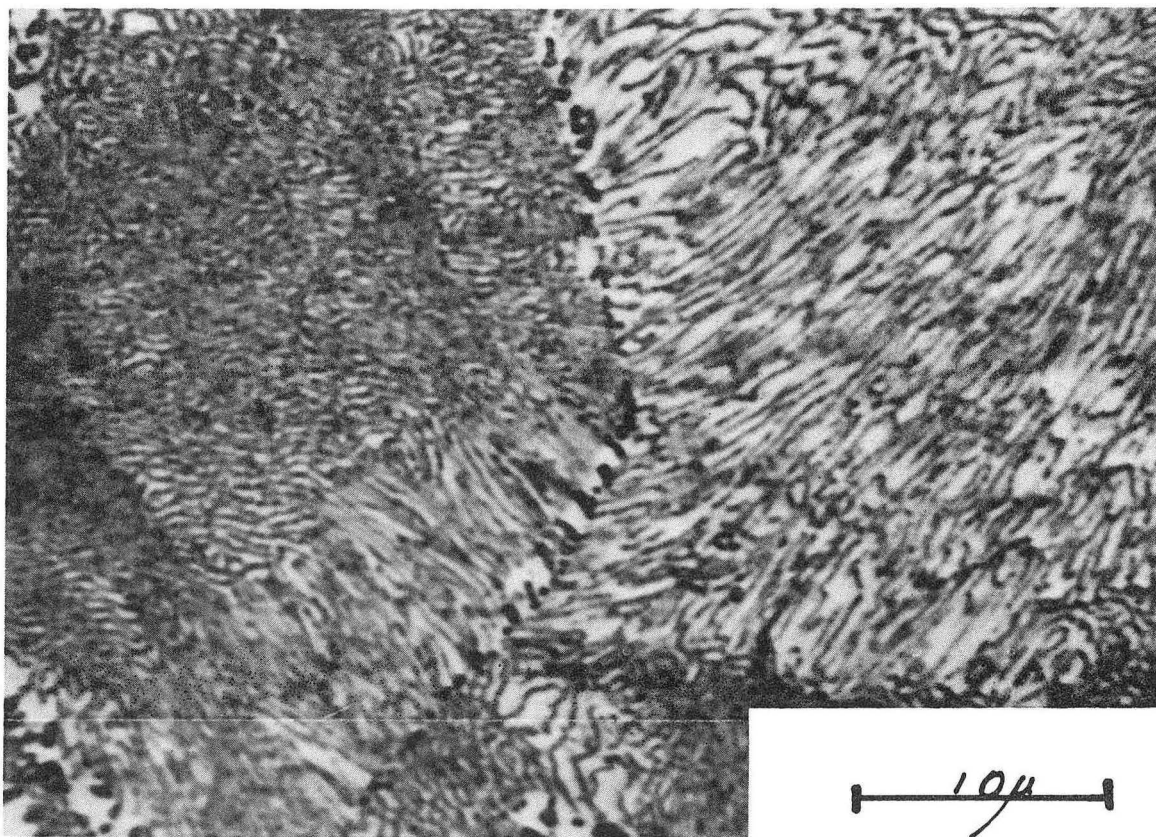
ZN-5612

Fig. 17 Micrograph of alloy 1 as solution-treated, quenched, and aged for 3912 min. at 1100°C.



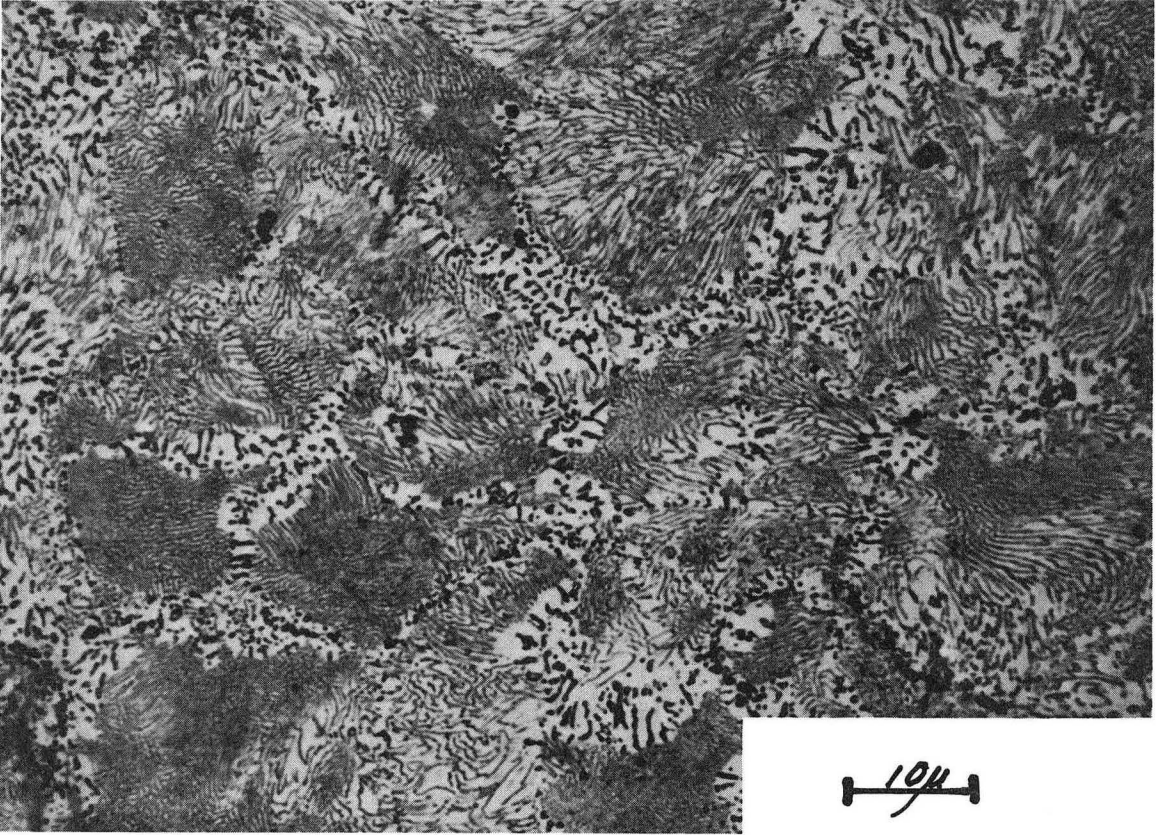
ZN-5666

Fig. 18 Micrograph of alloy 1 as solution-treated, quenched, and aged  
a) b) c)  
for 10,332 min. at 1100°C.

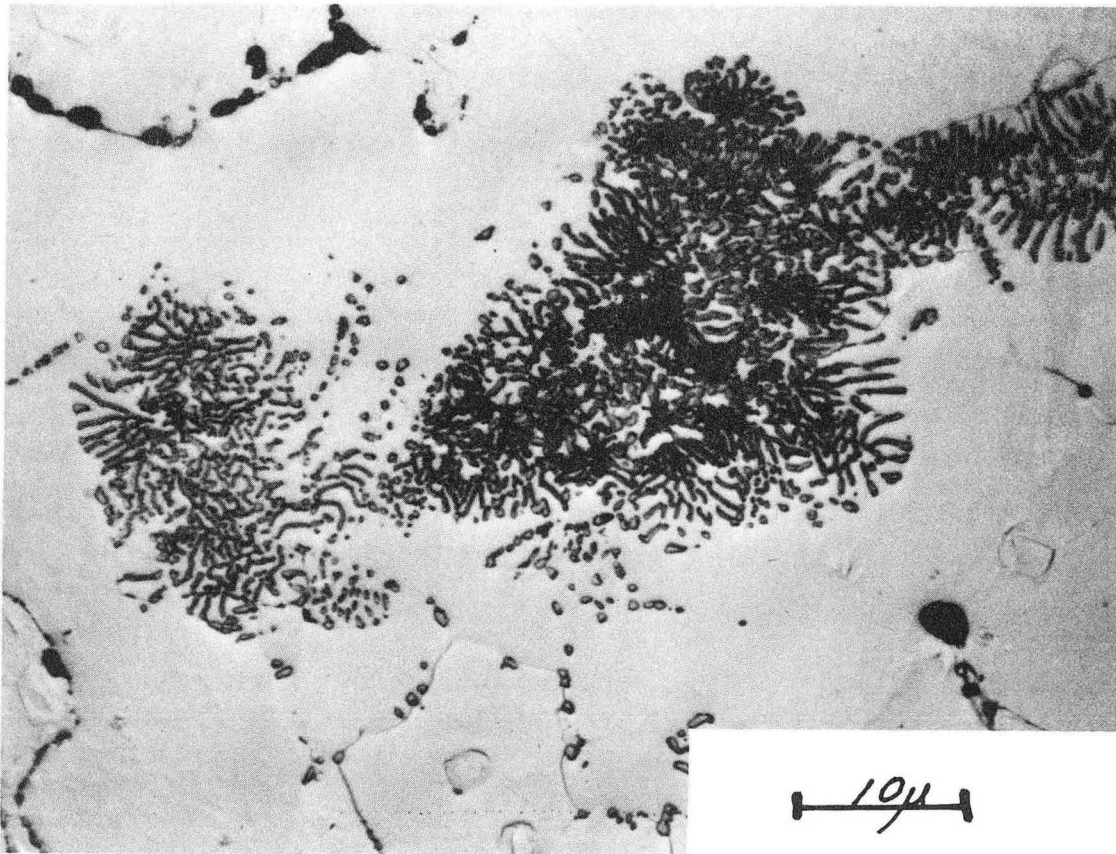


ZN-5619



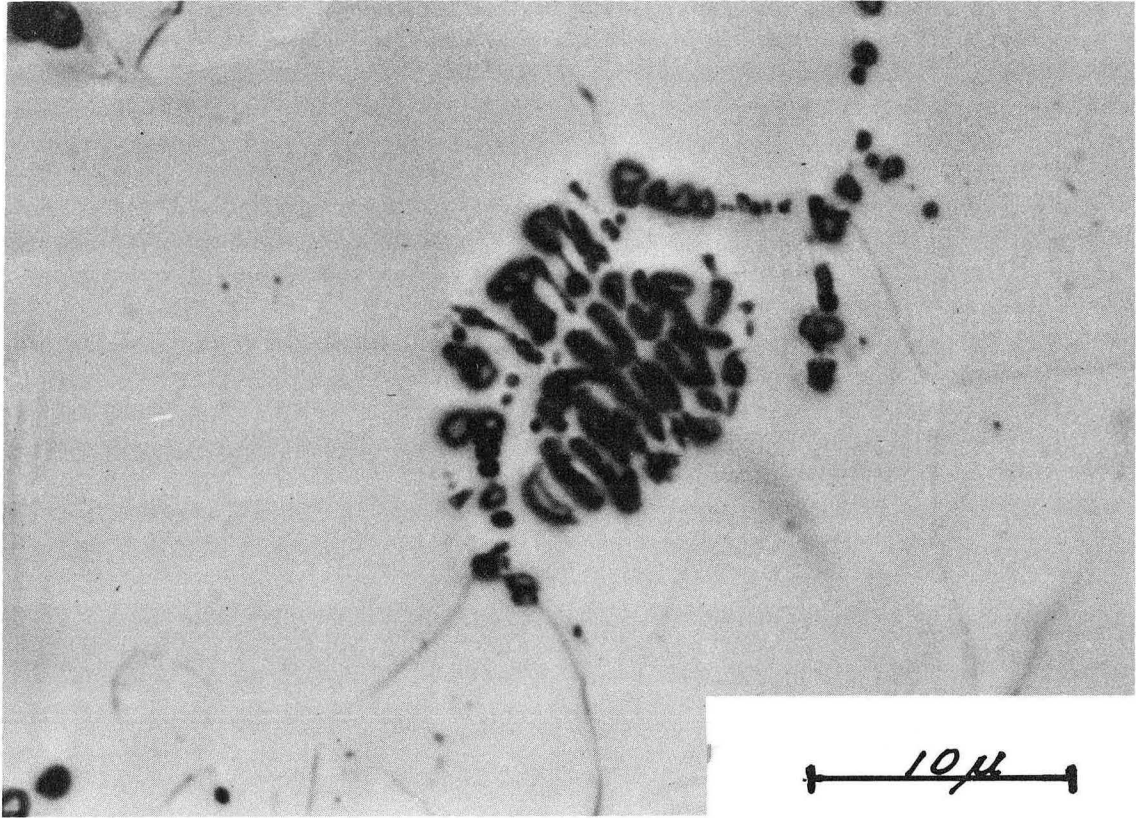


ZN-5668



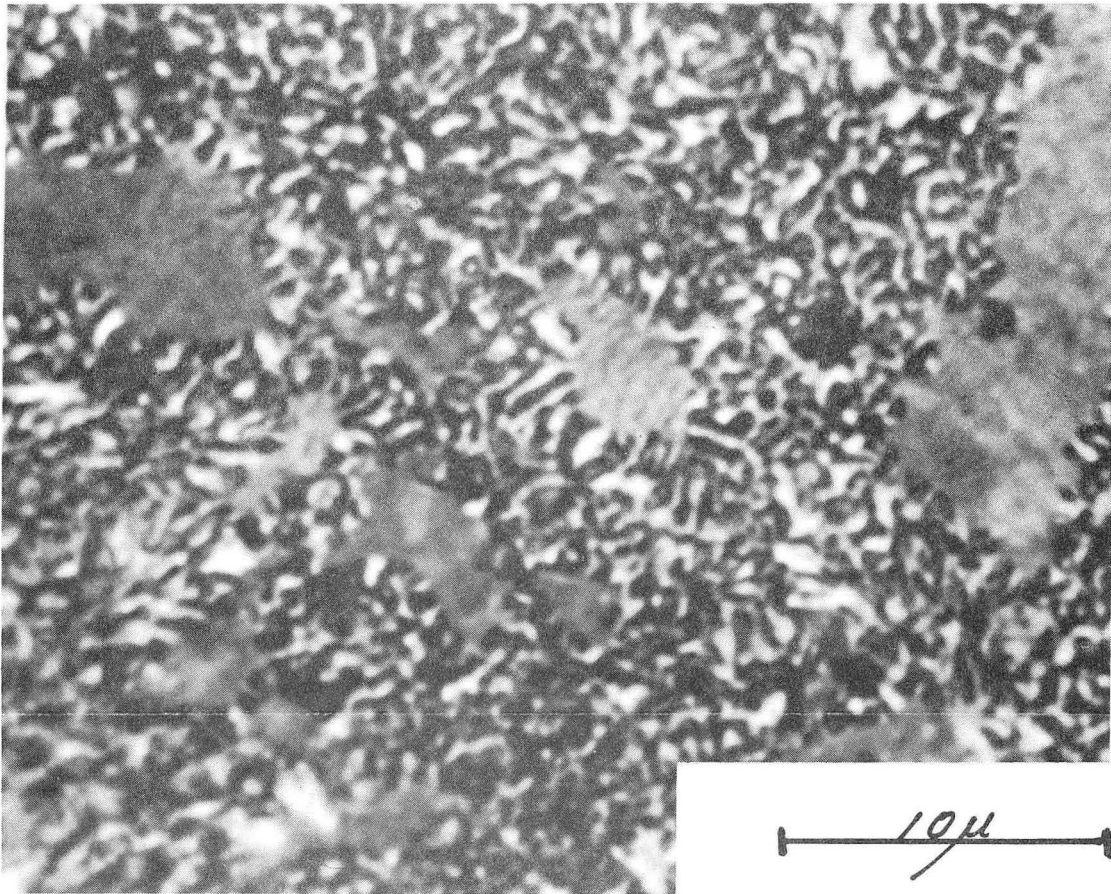
ZN-5621

Fig. 19 Micrograph of alloy 1 as solution-treated, quenched, and aged  
a) b)  
for 920 min. at 1300°C.



ZN-5618





ZN-5617

Fig. 20 Micrograph of alloy 2 as solution-treated, quenched, and aged for 2000 min. at 1000°C.

This report was prepared as an account of Government sponsored work. Neither the United States, nor the Commission, nor any person acting on behalf of the Commission:

- A. Makes any warranty or representation, expressed or implied, with respect to the accuracy, completeness, or usefulness of the information contained in this report, or that the use of any information, apparatus, method, or process disclosed in this report may not infringe privately owned rights; or
- B. Assumes any liabilities with respect to the use of, or for damages resulting from the use of any information, apparatus, method, or process disclosed in this report.

As used in the above, "person acting on behalf of the Commission" includes any employee or contractor of the Commission, or employee of such contractor, to the extent that such employee or contractor of the Commission, or employee of such contractor prepares, disseminates, or provides access to, any information pursuant to his employment or contract with the Commission, or his employment with such contractor.

